High-field multifrequency ESR in the S=5/2 kagome-lattice antiferromagnet KFe[subscript 3}(OH)[subscript 6](SO[subscript 4])[subscript 2]

High-field multifrequency ESR in the $S = \frac{5}{2}$ kagome-lattice antiferromagnet $KFe_3(OH)_6(SO_4)_2$

T. Fujita, H. Yamaguchi,* S. Kimura,† T. Kashiwagi,‡ and M. Hagiwara§
KYOKUGEN, Osaka University, Machikaneyama 1-3, Toyanaka, Osaka 560-8531, Japan

K. Matan
Department of Physics, Mahidol University, 272 Rama VI Road, Ratchathewi, Bangkok 10400, Thailand

D. Grohol
The Dow Chemical Company, Core R&D, Midland, Michigan 48674, USA

D. G. Nocera
Department of Chemistry, Massachusetts Institute of Technology, Cambridge, Massachusetts 02139, USA

Y. S. Lee
Department of Physics, Massachusetts Institute of Technology, Cambridge, Massachusetts 02139, USA
(Received 20 September 2011; revised manuscript received 11 January 2012; published 6 March 2012)

We have performed high-field multifrequency electron spin resonance (ESR) and high-field magnetization measurements in magnetic fields H of up to 53 T on single crystals of the kagome-lattice antiferromagnet $KFe_3(OH)_6(SO_4)_2$. We have analyzed the magnetization curve and the ESR excitation modes for $H \| c$ by using two kinds of anisotropy origins, the Dzyaloshinsky-Moriya (DM) interactions and the single-ion anisotropy, the former of which is inevitable in a kagome-lattice antiferromagnet. We obtained good agreement between experiment and calculation for the case of the DM interactions. In addition, we have clarified the origin of a field-induced metamagnetic transition observed in the magnetization curve and determined the intraplane and interplane exchanges and the DM interaction parameters.

DOI: 10.1103/PhysRevB.85.094409 PACS number(s): 76.30.−v, 75.10.Hk, 75.50.Ee

I. INTRODUCTION

Frustrated spin systems provide a rich variety of magnetic states, such as spin-liquid,[1–3] spin-nematic,[4,5] and spin-ice[6,7] states. In particular, kagome-lattice antiferromagnets have recently attracted considerable attention as highly frustrated spin systems because the corner-sharing arrangement leads to higher degeneracy of the ground state than the edge-sharing arrangement in triangular lattices. The Heisenberg antiferromagnet on the kagome lattice with the nearest-neighbor interactions is one of the most interesting subjects because we expect the realization of a kind of "spin-liquid" ground state.

In a classical limit, the ground state is expected to possess two possible spin structures, $q = 0$ and $\sqrt{3} \times \sqrt{3}$, both of which satisfy the "120° spin structure." Furthermore, the classical ground state has a continuous degeneracy due to the "weathervane" rotation of the spins, and thus no long-range order is expected even at zero temperature.[8–11] However, it has been also shown that thermal or quantum fluctuations could lift some of the continuous degeneracy known as "order by disorder." Theoretical studies for a large spin value predicted that the ground state has the $q = \sqrt{3} \times \sqrt{3}$ spin structure, which is selected by quantum fluctuations.[3] On the other hand, for a small spin value, a disordered ground state such as a resonating valence bond[12] (RVB) state is expected to be observed.

The number of reported experimental studies of Heisenberg kagome-lattice antiferromagnets is not large because model compounds are usually difficult to synthesize in single-crystal form. Recently, some experimental results of $S = 1/2$ Heisenberg kagome-lattice antiferromagnet compounds, which are $[Cu_3(titmb)_2(OCOCH_3)_6]H_2O$,[13] herbertsmithite $ZnCu_3(OH)_6Cl_2$,[14–17] volborthite $Cu_3V_2O_7(OH)_2{\cdot}2H_2O$,[18,19] vesignieite $BaCu_3V_2O_8(OH)_2$,[20,21] and $A_2Cu_3SnF_{12}$ (A = Rb, Cs),[22–24] were reported. They, however, are far from ideal kagome-lattice antiferromagnets because of lattice distortion, partial substitution of nonmagnetic ions, and considerably large amounts of impurities.

By contrast with these kagome-lattice antiferromagnets, jarosites, which have a chemical formula $AM_3(OH)_6(SO_4)_2$,[25] where A is a monovalent cation and M is a trivalent cation, have been considered as ideal kagome lattices. Many kinds of jarosite compounds are listed by the combination of A^+(Na^+, Rb^+, Ag^+, Tl^+, NH_4^+, H_3O^+) and M^{3+}(Fe^{3+}, Cr^{3+}, V^{3+}, Al^{3+}, Ga^{3+}, In^{3+}) ions. $KFe_3(OH)_6(SO_4)_2$ with Fe^{3+} ($S = 5/2$), abbreviated as K-Fe-jarosite, is one of the model compounds of a typical classical Heisenberg kagome-lattice antiferromagnet. Magnetic susceptibilities of the K-Fe-jarosite follow the Curie-Weiss law at high temperatures with negative Weiss temperature $\Theta \sim -800$ K,[26] indicating that the nearest-neighbor interaction is antiferromagnetic. Neither the lattice distortion of the kagome plane nor the partial substitution of nonmagnetic ions has been reported and, thus, this jarosite is regarded as one of the ideal frustrated spin systems. However, the K-Fe-jarosite undergoes a three-dimensional (3D) long-range order below the Neél temperature (T_N) 65 K.[26] The frustration parameter $f = |\Theta|/T_N$ is about 12, indicating that this compound is highly frustrated.

The magnetic structure below T_N was determined to be the $q = 0$ spin structure with +1 spin chirality by neutron

scattering experiments,[27] where spin chiralities $+1$ and -1 are defined as clockwise and counterclockwise spin rotations in the view of clockwise spin-site rotation, respectively. High-quality large single crystals of K-Fe-jarosite, which were made by recent development of the precipitation reaction method,[28] enable us to investigate the details of kagome physics without any assumption. In a previous study,[29] magnetic susceptibilities and magnetization indicated the presence of a weak ferromagnetism along the c direction. Recent theoretical work[30] showed that the Dzyaloshinsky-Moriya (DM) interaction would induce such canting moments, and the magnetic structure of the K-Fe-jarosite could be explained by the DM interactions. A neutron research using a single crystal of K-Fe-jarosite[31] provided details of spin excitations. Spin-wave excitations were observed in the inelastic neutron scattering experiments.

As already mentioned, the K-Fe-jarosite forms an ideal kagome lattice, which remains undistorted down to sufficiently low temperatures. There are few previous reports of the experiments on a single crystal of a kagome-lattice antiferromagnet.[29,31] This paper provides an in-depth study on a classical Heisenberg kagome-lattice antiferromagnet using a single crystal. ESR is mostly useful for evaluating the perturbation parameters such as the DM interaction, which inevitably results from the symmetry of the kagome lattice. Thus, it is important to evaluate the DM components from experiment because the magnitude of the DM interaction is key to understanding the nature of the K-Fe-jarosite kagome-lattice antiferromagnet. We performed magnetization and ESR measurements in magnetic fields of up to about 50 T with pulsed magnets.

In a previous paper,[29] magnetic phase transition was observed near T_N and was not observed at low temperatures because of the limit of magnetic field. The successive paper[32] reported the results of high-field magnetization at sufficiently low temperatures. Since the combination of high-field magnetization and ESR results enables us to determine the physical parameters precisely, we have performed magnetization measurements at 4.2 K in high magnetic fields at our high magnetic field laboratory.

The paper is organized as follows. In Sec. II, crystal structures of K-Fe-jarosite and experimental methods are described. Then, experimental results of magnetization and ESR measurements are reported in Sec. III, followed by their analyses assuming two kinds of anisotropy origins in Sec. IV. We discuss how to determine the parameters and the validity. The observed magnetic structure in K-Fe-jarosite is discussed with a theory including the DM interaction in a classical kagome-lattice antiferromagnet. The final section is devoted to the conclusion.

II. EXPERIMENT

A. Crystal structure

A single-crystal sample ($\sim 2 \times 2 \times 0.5$ mm^3) of K-Fe-jarosite used in this study was prepared by a redox-based hydrothermal method. The details of the single-crystal synthesis were reported in Refs. 28 and 29. The K-Fe-jarosite belongs to a rhombohedral system with $R\bar{3}m$ symmetry, and lattice constants are $a = b = 7.30$ Å and $c = 17.09$ Å at room temperature.[33] The crystal structure consists of kagome layers of Fe^{3+} ions in the ab plane. These planes stack along the c axis, separated by nonmagnetic layers of SO_4^{2-} and K^+, as shown in Fig. 1(a). As depicted in Fig. 1(b), the Fe^{3+} ions are coordinated with two oxygen atoms from SO_4^{2+} and four oxygen atoms from OH^- ions to form slightly distorted octahedrons. Such anisotropic structure suggests that K-Fe-jarosite has stronger interactions in the layers than those along the c axis. Figures 1(c) and 1(d) indicate two types of arrangements of FeO_6 octahedron in this compound. The

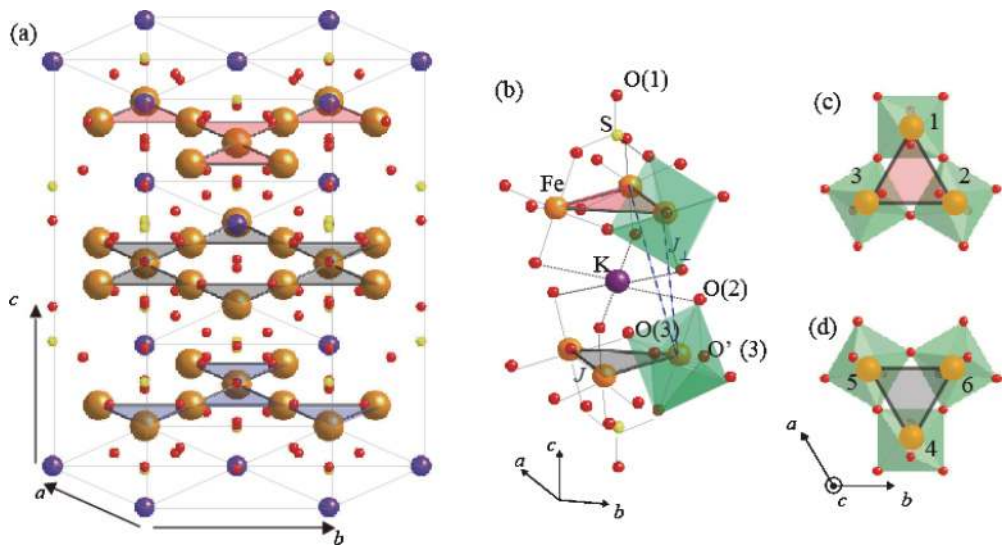

FIG. 1. (Color online) (a) Crystal structure of K-Fe-jarosite. Hydrogen atoms are omitted for clarity. Fe^{3+} ions form a kagome lattice in the ab plane. (b) Arrangement of triangles in the kagome lattice along the c axis and the local environment around Fe^{3+} ions. The kagome Fe^{3+} layers are separated by planes of nonmagnetic K^+ and SO_4^{2-} ions. (c) and (d) Arrangement of the FeO_6 octahedron in the nearest triangular layers along the c axis. The principal axis of the octahedron is tilted from the c axis, and the tilting directions of the octahedron in (c) and (d) are opposed to each other.

tilting directions of the octahedron on each triangle against the c axis change alternatively with the layers along the c axis.

B. Experimental methods

Pulsed field ESR measurements were conducted in magnetic fields (H) of up to 53 T at temperatures between 1.3 and 300 K by using our pulsed field ESR apparatus equipped with a nondestructive pulse magnet, a far-infrared laser (Edinburgh Instruments, FIRL100), several kinds of Gunn Oscillators, which cover the frequency range between 50 GHz and 2 THz, and an InSb detector (QMC Instruments). The ESR measurements at 1.6 K and frequencies below 500 GHz in static magnetic fields of up to 14 T were also performed by utilizing a superconducting magnet (Oxford Instruments) and a vector network analyzer (AB millimetre, MVNA). High-field magnetization measurements at 4.2 K in pulsed magnetic fields of up to 53 T were carried out with a nondestructive pulse magnet. The magnetization was measured with an induction method using a pick-up coil. The magnetization at 4.2 K in a magnetic field of up to 7 T was also measured with a superconducting quantum interference device (SQUID) magnetometer (Quantum Design, MPMS-XL7) for the correction of magnetization measured in pulsed magnetic fields. All the experiments were carried out at KYOKUGEN in Osaka University.

III. EXPERIMENTAL RESULTS

A. High-field magnetization

Figure 2 shows a magnetization curve at 4.2 K for $H \| c$. The curve with a broken line drawn by the raw data indicates a bending with a convex curvature at low fields, which is probably caused by paramagnetic impurities. Thus, we subtract the paramagnetic contribution from the raw data, assuming the Brillouin function for $S = 5/2$ with the impurity content of ~0.4%. Then, the magnetization curve by the subtracted data

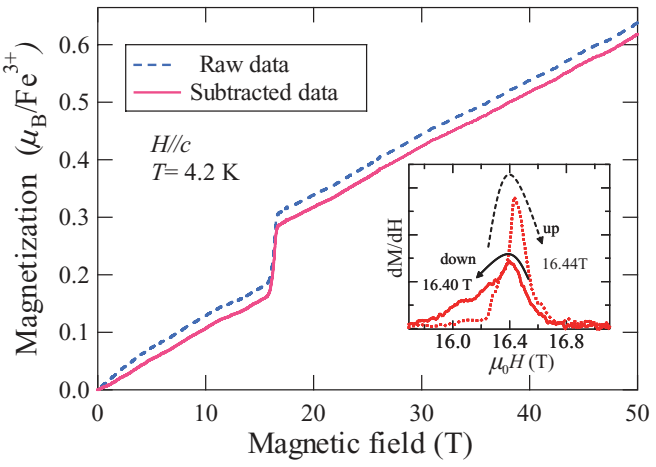

FIG. 2. (Color online) Magnetization curve of K-Fe-jarosite at 4.2 K for $H \| c$ (field descending process). Broken and solid lines are the raw magnetization curve, and the magnetization subtracted the contribution of paramagnetic impurity from the raw data, respectively. The inset shows the field derivative of the magnetization at 4.2 K for $H \| c$.

increases almost linearly with increasing field as shown with a solid line in Fig. 2. A steep increase, which corresponds to the magnetic transition reported previously,[29,32] is observed at about 16 T. This abrupt increase of the magnetization is believed to result from a change from antiferromagnetically aligned canted moments along the c axis to ferromagnetically aligned ones. The inset of Fig. 2 shows the field derivative of magnetization curve (dM/dH) observed at 4.2 K for $H \| c$. The dM/dH shows a distinct peak around $H_c = 16.4$ T, which we define as the critical field (H_c). Since there is a hysteresis near H_c, this magnetic transition must be a first-order phase transition.

B. High-field ESR

Figures 3(a) and 3(b) show the frequency dependence of the ESR absorption spectra for $H \| c$ at 1.6 K in static magnetic fields and those at 1.3 K in pulsed magnetic fields, respectively. We observed some broad resonance signals indicated by the arrows and some sharp anomalies indicated by the open circles. All the resonance fields are plotted in the frequency-field plane as shown later in Figs. 6(b) and 8(b). We detected ESR modes with zero-field gaps of about 1600 and 350 GHz. The energy branches with the zero-field gaps were observed in the previous neutron scattering experiments.[31] We conclude that the observed ESR modes correspond to the excitation modes at the Γ point.

IV. ANALYSES

A. Dzyaloshinsky-Moriya model

First, we analyze the frequency dependence of the ESR resonance fields and the magnetization curve, both for $H \| c$ orientation. In this task, we use the following spin Hamiltonian, which we call the DM model Hamiltonian because of the inclusion of the DM term as the anisotropy origin

$$\mathcal{H} = J\sum_{\langle ij\rangle} S_i \cdot S_j + J_\perp \sum_{\langle lm\rangle} S_l \cdot S_m + \sum_{\langle ij\rangle} d_{ij} \cdot S_i \times \cdot S_j - g\mu_B \sum_i S_i \cdot H, \quad (1)$$

where J is the nearest-neighbor exchange constant in the ab plane, $\sum_{\langle ij\rangle}$ the summation over pairs of the nearest-neighbor spins, S_i $S = 5/2$ spin operator of Fe^{3+} at i site, $J_\perp$ the interplane exchange constant, $\sum_{\langle lm\rangle}$ the summation over pairs of the nearest-neighbor spins along the c axis, d_{ij} the DM vector between i- and j-site spins, g the g value of Fe^{3+} spin, μ_B the Bohr magneton, and H the external magnetic field. When the magnetic ions form a kagome lattice, the DM interaction is imperative because of no inversion center between the neighboring sites. The direction of the DM vector is constrained and follows the rules described by Moriya.[36] The DM vectors exist in the mirror plane between the nearest i and j sites in the kagome lattice as shown in Fig. 4. Here, we divide the DM vector into two components: d_p, the in-plane component, and d_z, the z component parallel to the c axis.

Elhajal *et al.*[30] and Yildirim *et al.*[37] discussed the DM interaction in a jarosite. The directions of the DM vectors are different in these reports. However, the definitions of

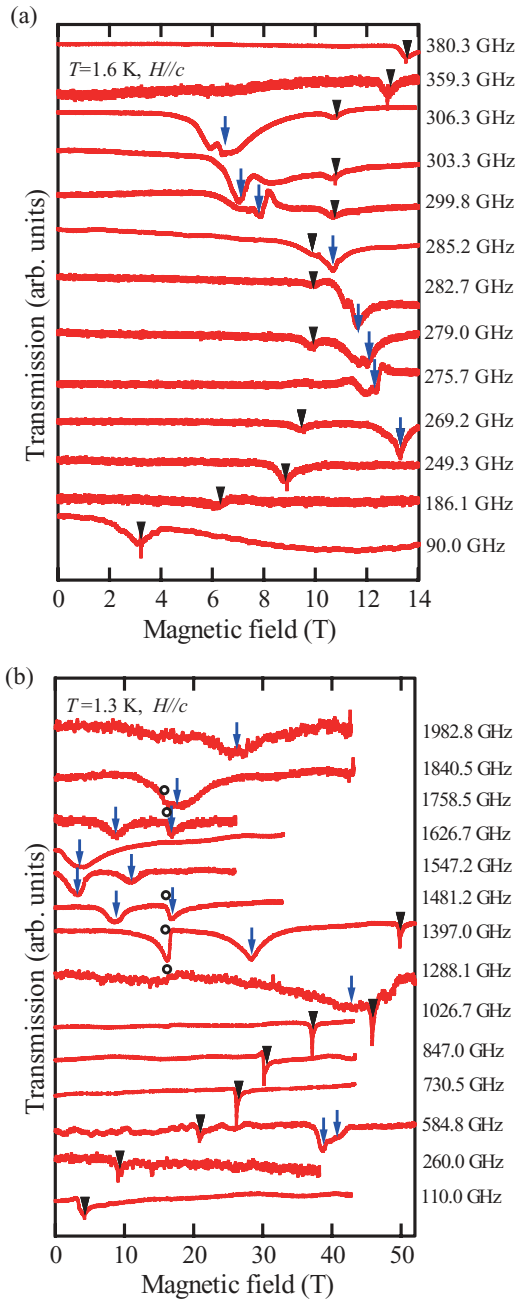

FIG. 3. (Color online) Frequency dependence of (a) ESR absorption spectra of K-Fe-jarosite for $H \| c$ at 1.6 K in static magnetic fields and (b) those at 1.3 K in pulsed magnetic fields. The arrows, inverted triangles, and circles indicate intrinsic ESR signals, paramagnetic signals from impurities, and a baseline anomaly caused by the magnetic transition, respectively.

the DM vectors are essentially identical. In this paper, we analyzed the experimental results based on Elhajal's definition, which is different from the definitions in Ref. 32. Elhajal *et al.* discussed theoretically the effects of d_z and d_p for a classical Heisenberg kagome-lattice antiferromagnet using a mean-field approximation and a classical Monte Carlo simulation. They argued that the d_z acts to create an easy-plane anisotropy. The coplanar magnetic structure is realized when this component exists, and the direction of the chirality vector

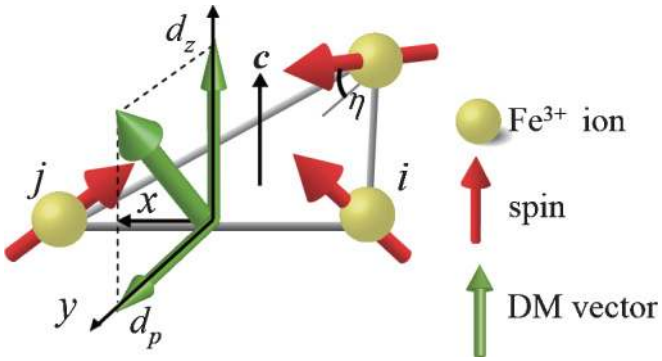

FIG. 4. (Color online) Dzyaloshinsky-Moriya (DM) vector (thick green vector) and spin-canted state (red vectors) in K-Fe-jarosite. The DM vector exists in the mirror plane between i and j sites. The green thin vectors indicate projective components of the DM vector to kagome plane (d_p) and to the c axis (d_z).

is determined by the sign of d_z. Accordingly, $d_z > 0$ and $d_z < 0$ stabilize positive and negative chirality, respectively. In the K-Fe-jarosite, the $q = 0$ structure with positive chirality was observed in powder neutron diffraction,[26] thus $d_z > 0$ acting on this system. Elhajal *et al.* also discussed that all the spins have a weak c-axis component when d_p is nonzero, resulting in a weak ferromagnetism and no global rotational degeneracy. Accordingly, magnetic behavior of the K-Fe-jarosite at low temperatures seems to be described by the DM interaction. Therefore, we carried out first the analyses by taking into account the DM interaction. It is, however, impossible to explain the arrangement of the spins along the c axis and magnetic transition found in the magnetization curve merely considering the intraplane exchange and the DM interactions. Hence, the weak ferromagnetic interlayer coupling $J_\perp$ is required for the analysis as indicated in Eq. (1). This term forces the spins to align in such a way that canted moments on two adjacent layers are directed opposite of each other, and the competition between the Zeeman energy and weak ferromagnetic interlayer coupling causes the spins on the alternating layers to rotate 180°.[32] As shown in Fig. 5, the spin structure below H_c can be described by a six-sublattice model, and the spin structure above H_c can be described by a three-sublattice model. Then, the free energy F is expressed by the following form using a mean-field approximation:

$$F = A\sum_{\langle ij\rangle} \boldsymbol{M}_i \cdot \boldsymbol{M}_j + B\sum_{\langle lm\rangle} \boldsymbol{M}_l \cdot \boldsymbol{M}_m + \sum_{\langle ij\rangle} \boldsymbol{dt}_{ij} \cdot \boldsymbol{M}_i \times \boldsymbol{M}_j - \sum_{i=1} \boldsymbol{M}_i \cdot \boldsymbol{H}. \quad (2)$$

Here, the coefficients and the vectors below H_c are given by $A = 12J/[N(g\mu_B)^2]$, $B = 12J_\perp/[N(g\mu_B)^2]$, $\boldsymbol{dt}_{ij} = 12\boldsymbol{d}_{ij}/[N(g\mu_B)^2]$, and $\boldsymbol{M}_i = Ng\mu_B\boldsymbol{S}_i/6$. Above H_c, they are written as $A = 6J/[N(g\mu_B)^2]$, $B = 6J_\perp/[N(g\mu_B)^2]$, $\boldsymbol{dt}_{ij} = 6\boldsymbol{d}_{ij}/[N(g\mu_B)^2]$, and $\boldsymbol{M}_i = Ng\mu_B\boldsymbol{S}_i/3$. N is the number of magnetic ions, and $\boldsymbol{M}_i$ are the magnetic moments on the ith sublattice.

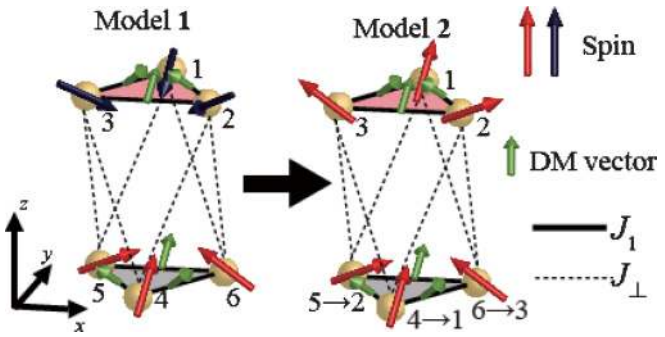

FIG. 5. (Color online) The detail of the interaction in K-Fe jarosite. Dzyaloshinsky-Moriya (DM) vector (thick green vector) and spin-canted state (red and blue vectors).

The magnetization curve is calculated from this free energy. We derive the resonance conditions by solving the equation of motion

$$\partial \boldsymbol{M}_i/\partial t = \gamma[M_i \times H_i], \tag{3}$$

where γ is the gyromagnetic ratio and H_i a mean-field applied on the ith sublattice moment given by

$$H_i = -\partial F/\partial M_i. \tag{4}$$

To solve the equation of motion, we use a method applied for ABX_3-type antiferromagnets.[34] Assuming precession motions of the sublattice moments around those equilibrium directions, we utilize the following expressions, which represent the motion of the ith sublattice moment:

$$M_i' = [|M_i|, \Delta M_{i\hat{y}} \exp(i\omega t), \Delta M_{i\hat{z}} \exp(i\omega t)], \tag{5}$$

where $\Delta M_{i\hat{y}}, \Delta M_{i\hat{z}} \ll |M_i|$, and $\hat{x}$, $\hat{y}$, and $\hat{z}$ are the principal axes of the coordinate system on each sublattice moment. The $\hat{x}$ axis is defined to be parallel to the direction of the each sublattice moment, and the $\hat{y}$ and $\hat{z}$ axes are perpendicular to that.

As shown in Fig. 6, we obtained good agreement between experiment and calculation using the following parameters: $J/k_B = 42.3$ K, $J_\perp/k_B = -9.66 \times 10^{-2}$ K, $d_p/k_B = 1.62$ K, $d_z/k_B = 1.97$ K, and $g_c = 2.00$. The details of determination of these parameters will be described in the next discussion section. The g value g_c is determined by ESR signal at 294 K (paramagnetic phase) as will be shown later in Fig. 9. The canting angle at 0 T is evaluated at 1.23°.

B. Crystal-field (CF) model

Next, we analyze the experimental data by the following spin Hamiltonian assuming single-ion anisotropies (D and E). We call this model a crystal-field (CF) model:

$$\mathcal{H} = J\sum_{\langle ij\rangle} S_i \cdot S_j + J_\perp \sum_{\langle lm\rangle} S_l \cdot S_m + D\sum_i \left(S_i^{z'}\right)^2 - E\sum_i \left\{\left(S_i^{x'}\right)^2 - \left(S_i^{y'}\right)^2\right\} - g\mu_B \sum_i S_i \cdot H, \tag{6}$$

where the z' and y' axes are taken to be parallel to O(2)-Fe-O(2) and to be in the ab plane for each Fe^{3+} ion, respectively. The x' axis is perpendicular to the both axes as shown in Fig. 7.

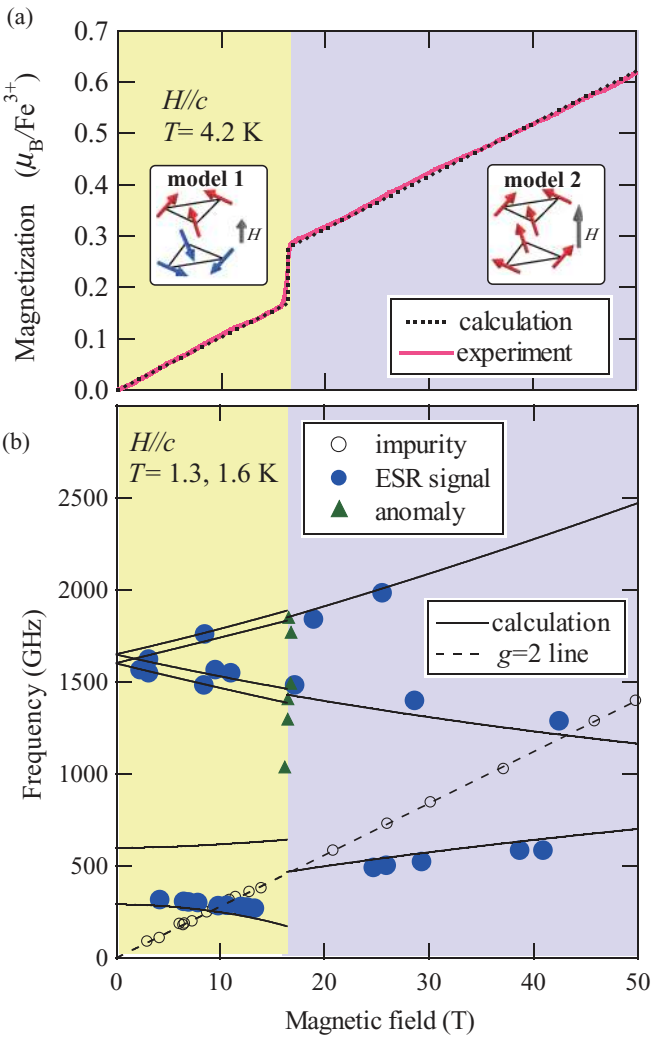

FIG. 6. (Color online) Comparison of the magnetization curve and the ESR modes of the K-Fe-jarosite between the experiment and the calculation for the DM model. (a) Solid and broken lines represent the experimental (4.2 K) and calculated (0 K) magnetization curves, respectively. The subtracted data in Fig. 2 is used as the experimental result. (b) Frequency-field plot of the resonance fields taken at 1.3 K in pulsed fields and at 1.6 K in static fields for $H \| c$. Closed and open circles and triangles denote the resonance fields of intrinsic signals, those of an impurity signal and an anomaly accompanied with the magnetic transition, respectively. The solid lines show the calculated ESR modes and the thin broken line represents a paramagnetic-resonance line.

The z' axis is tilted from the c axis about 20°. The single-ion anisotropies were discussed in a previous paper on powder neutron scattering experiment.[26] When $D > 0$, we have an easy-plane anisotropy and E determines the direction of spin in the $x'y'$ plane. Large-D and small-E values are expected from the crystal structure because the distortion of the FeO_6 octahedron along the z' axis is larger than that in the $x'y'$ plane. Because of the positive D, the magnetic moments tend to lie in the $x'y'$ plane, which is slightly tilted from the ab plane. The positive E makes the magnetic moments direct to the x' axis. Therefore, the magnetic system chooses the $q = 0$ structure with +1 spin chirality and ferromagnetic component.

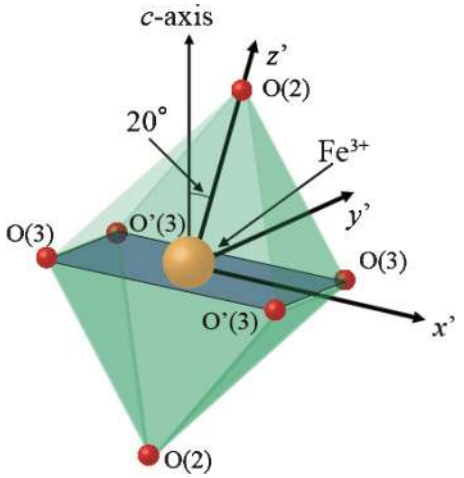

FIG. 7. (Color online) Local environment and coordination around Fe^{3+}. The local principal z' axis is parallel to the O(2)-Fe-O(2) and is tilted from the c axis. The y' axis is in the ab plane and the x' axis is perpendicular to the y' and z' axes.

In this manner, the single-ion anisotropies may generate spin arrangement in this study. The free energy F is expressed by the following form using a mean-field approximation:

$$F = A\sum_{\langle ij\rangle} M_i \cdot M_j + B\sum_{\langle lm\rangle} M_l \cdot M_m + K\sum_i \left(M_{CFi}^{z'}\right)^2 - C\sum_i \left\{\left(M_{CFi}^{x'}\right)^2 - \left(M_{CFi}^{y'}\right)^2\right\} - \sum_{i=1} M_i \cdot H. \quad (7)$$

Here, the coefficients that are different from those in the previous section are given by $K = 6D/[N(g\mu_B)^2]$, $C = 6E/[N(g\mu_B)^2]$ below H_c, and by $K = 3D/[N(g\mu_B)^2]$, $C = 3E/[N(g\mu_B)^2]$ above H_c.

The magnetization is calculated in the same way as in the previous section. As shown in the calculation # 1 in Figs. 8(a) and 8(b), we obtain good agreement between experiment and calculation for the magnetization curve using the following parameters: $J/k_B = 42.3$ K, $J_\perp/k_B = -9.66 \times 10^{-2}$ K, $D/k_B = 8.29$ K, $E/k_B = 0.522$ K and the same g_c value as in the analysis of the DM model. The canting angle at 0 T is evaluated at 1.21°. However, poor agreement is attained between experiment and calculation for the ESR modes, especially the high-frequency ones. We have also analyzed experimental results so that the fitting of ESR modes might be improved as much as possible in the CF model. The analytical results are shown by the calculation # 2 in Figs. 8(a) and 8(b). For this fitting, we use the following parameters: $J/k_B = 42.3$ K, $J_\perp/k_B = -5.51 \times 10^{-2}$ K, $D/k_B = 4.64$ K, $E/k_B = 0.322$ K, and $g_c = 2.00$. The canting angle at 0 T is evaluated at 0.70°. The agreement between the calculated and the experimental magnetization curves after the transition is not good. Accordingly, we have found that a large-D value is required to explain the large magnetization jump, while a smaller-D value is needed for the fit of the high ESR modes. Hence, both the high ESR modes and the magnetization curve can not be reproduced by the same parameters.

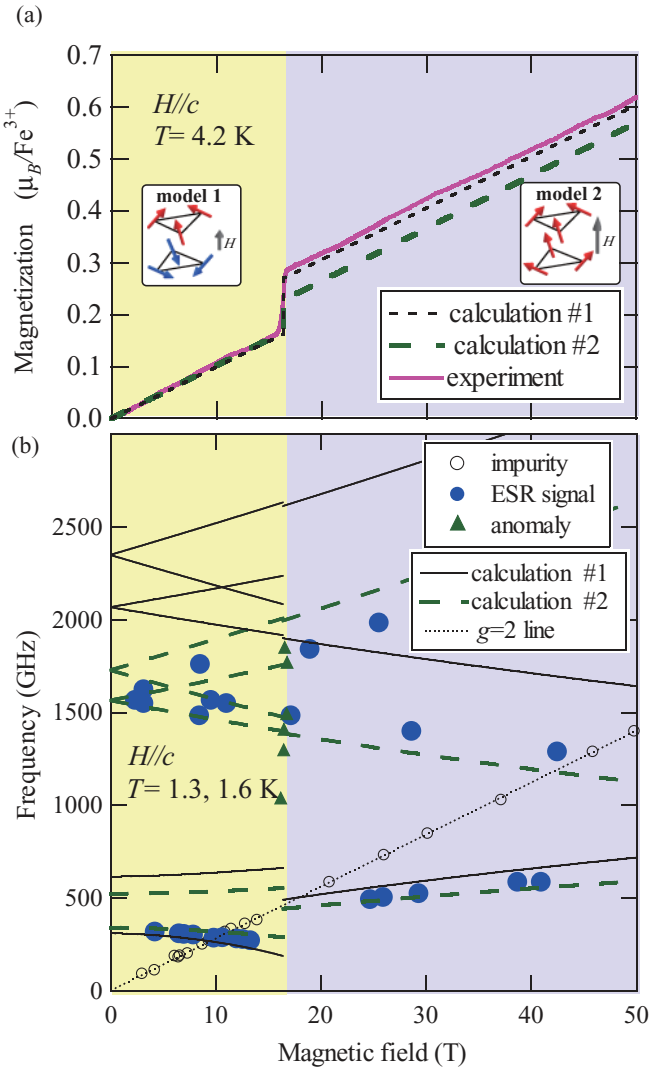

FIG. 8. (Color online) Comparison of the magnetization curve and the ESR modes of the K-Fe-jarosite between experiment and calculation for the CF model. (a) Solid line is the experimental magnetization curve (4.2 K). Thin black dotted (calculation #1) and thick green broken (calculation #2) lines are calculated (0 K) magnetization curves. (b) Frequency-field plot of the resonance fields taken at 1.3 K in pulsed fields and at 1.6 K in static fields for $H \| c$. The symbols are identical to those in Fig. 6(b). The black solid and thick green broken lines show the calculated ESR modes using the same parameters as in the calculations #1 and #2, respectively. The thin black dotted line represents a paramagnetic-resonance line with $g = 2$.

V. DISCUSSION

First, we discuss the validity of the DM model used to analyze the experimental results. In the analysis, we determine the J value from the slope of the magnetization curve (the solid line in the upper panel of Fig. 2) because the slope is proportional to $1/J$. We assume that the magnetic structure changes from the model 1 to 2 with an umbrella structure upon increasing magnetic field as illustrated in the insets of Figs. 6(a) and 8(a). The magnetic transition observed at 16.4 T is interpreted as a flop of the weak ferromagnetic component.

The relational expression[30] between the canting angle η and the intraplane exchange and DM parameters is given by

$$\tan 2\eta = \frac{2d_p}{(\sqrt{3}J + d_z)}. \quad (8)$$

When $J \gg d_z$, it is possible to approximate $\tan 2\eta = 2d_p/\sqrt{3}J$. The lowest zero-field ESR mode, which should be equivalent to the lowest zone-center spin-wave gap in the spin-wave dispersion, is described by $S\sqrt{12}|d_p|$.[31] Therefore, we adjust the value of d_p to meet both the magnitude of the magnetization step at the transition field and the zero-field value of the lowest ESR mode. Additionally, we evaluate the d_z from zero-field gap of the higher ESR mode. Then, we extract the value of $J_\perp$ from the comparison of the free energies between the models 1 and 2. In this analysis, we expect the energy crossing to occur at 16.4 T, where the dM/dH shows a distinct peak. This field-induced transition is explained by a competition between the interlayer coupling $J_\perp$ and the Zeeman energy. The following relation is given in Ref. 29: $H_c S \sin\eta = 2S^2|J_\perp|$. Since $\sin\eta$ is very small, H_c becomes large in spite of small $J_\perp$.

In the analyses of the CF model, we evaluate the J and $J_\perp$ values in the same manner as the DM model. We also determine the value of single-ion anisotropy constants D and E from the magnetization jump and the zero-field gap of the ESR modes. But, the magnetization jump and the high ESR modes are not simultaneously reproduced as we described in Sec. IV. The D value evaluated in this analysis is also too large in typical inorganic materials. It is generally accepted that the D and E values are small for Fe^{3+} ($L = 0$) except for a special ligand field environment such as met-myoglobin.[35] In addition, we performed the calculations including higher-order spin Hamiltonian term $a(S_x^4 + S_y^4 + S_z^4)$. However, the calculated results are far from the experimental ones, and thus the fits are not improved. From these considerations, we conclude the CF model is not suitable for this sample.

Next, we discuss the DM components determined by these analyses. In Table I, the magnitudes of the DM components evaluated in K-Fe-jarosite and other systems are summarized. In most kagome-lattice compounds, their DM components are of the order of 1 K. The magnitude of the d vector $|d|$ is roughly given by $|d| \sim (\Delta g/g)J$ (Ref. 36) where Δg is the difference of g values in the systems. As shown in Fig. 9, the g-value anisotropy is quite small from the observed paramagnetic resonance signals, and almost equivalent g values are obtained for the a axis ($g_a = 2.01 \pm 0.01$) and the c axis ($g_c = 2.00 \pm 0.01$). The magnitude of the DM vector is evaluated to be $|d| \sim (\Delta g/g)J = 0.275$ K, which is about one tenth of the value obtained from our analysis. The g-value anisotropy of about 0.12 is required to reproduce the size of DM vector evaluated by the analysis. However, it makes little sense that such g-value anisotropy is present in Fe^{3+} ions with the orbital momentum $L = 0$. This is the only contradiction point in the analyses by the DM model. However, we can conclude that the DM model is more suitable than the CF model for K-Fe-jarosite.

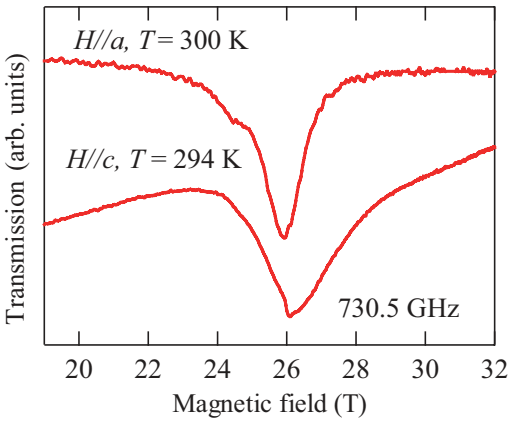

FIG. 9. (Color online) EPR signals of K-Fe-jarosite at 730.5 GHz for $H \| c$ and $H \| a$ at designated temperatures.

Finally, we discuss the ground state of Heisenberg kagome-lattice antiferromagnets. As described in the Introduction, theoretical studies predicted that the ground state has a $\sqrt{3} \times \sqrt{3}$ 120° spin structure for a Heisenberg kagome-lattice antiferromagnet with a large spin value, and has a "spin-liquid'-like resonating valence bond (RVB) state with a small spin value. A long-range order (LRO) was observed in most experimental studies on Heisenberg kagome-lattice antiferromagnets, such as Cr-jarosite (Cr: $S = 3/2$),[28,39] hexagonal tungsten bronze(HTB)-type FeF_3 (Fe: $S = 5/2$),[40] and $A_2Cu_3BF_{12}$ type materials ($Cs_2Cu_3ZrF_{12}$, $Cs_2Cu_3SnF_{12}$, and $Cs_2Cu_3HfF_{12}$ (Cu: $S = 1/2$).[23] Neutron scattering studies on (HTB)-type FeF_3 clarified the $q = 0$ structure below T_N.[40] In addition, previous studies on Cr-jarosite and some $A_2Cu_3BF_{12}$ indicated the presence of weak ferromagnetism.[23,39] The observed $q = 0$ structure and weak ferromagnetism in K-Fe-jarosite must be ascribed to positive d_z and d_p, respectively. When the spin is large enough, and finite interplane interactions exist in a real compound, it exhibits a LRO. In such case, the DM interaction works as the main perturbation term to determine the ground-state spin structure below T_N.

On the other hand, studies carried out on herbertsmithite (Cu: $S = 1/2$), volborthite (Cu: $S = 1/2$), vesignieite

TABLE I. The comparison of the DM components in kagome-lattice samples.

Sample	$\|d_z\|$ (K)	$\|d_p\|$ (K)	$\|d\|$ (K)	$(\Delta g/g)J$ (K)
K-Fe-jarosite (this study)	1.62	1.97	2.55	0.275
K-Fe-jarosite (Ref. 31)	2.27	2.29	3.22	
Ag-Fe-jarosite (Ref. 32)	1.97	2.09	2.87	
Herbertsmithite (Ref. 38)	15	2	15.1	30.2
Cs_2Cu_3HfF (Ref. 23)		4.52		70.9
Cs_2Cu_3ZrF (Ref. 23)		6.10		61.6

(Cu: $S = 1/2$), and $Rb_2Cu_3SnF_{12}$ (Cu: $S = 1/2$) reported no LRO down to sufficiently low temperatures, and thus these materials seemed to realize some kinds of "quantum spin-liquid state" or "quantum spin-solid state." Recently, Cépas *et al.* theoretically investigated the effect of the DM interaction in the $S = 1/2$ kagome-lattice antiferromagnet and found a quantum critical point between a moment-free phase and an antiferromagnetic LRO one around $d_z \sim 0.1J$.[41] Accordingly, it is expected that the ground state of a Heisenberg kagome-lattice antiferromagnet is altered drastically by the DM interaction, and the value of spin.

VI. CONCLUSION

We have performed high-field magnetization and ESR measurements on a single-crystal sample of K-Fe-jarosite, which is one of the typical classical Heisenberg kagome-lattice antiferromagnets. We observed a number of ESR branches at $T = 1.3$ and 1.6 K, and a stepwise magnetization at 4.2 K for $H \| c$. We conclude that the DM interaction is the most dominant perturbation term that works in this system from the analysis of the experimental results. Our experimental results (magnetization and ESR) are successfully explained by the model having the DM interaction and the interplanar interaction, and the following parameter values were obtained: $J/k_B = 42.3$ K, $d_p/k_B = 1.62$ K, $d_z/k_B = 1.97$ K, $J_\perp/k_B = -9.66 \times 10^{-2}$ K, and $g_c = 2.00$. The magnetic transition at 16.4 T is caused by the change of spin structure, which arises from the competition between the DM, the interplanar, and the Zeeman interaction.

ACKNOWLEDGMENTS

We thank T. Kimura for the use of Laue photography apparatus. This work was supported by Grants-in-Aid for Scientific Research (No. 20340089), and the Global COE Program (Core Research and Engineering of Advanced Materials-Interdisciplinary Education Center for Materials Science) (No. G10) from the MEXT, Japan.

APPENDIX A

As already mentioned in Sec. IV A, we analyzed experimental results by the DM model using a mean-field approximation. In this appendix, we describe the details of the analysis. In the case of model 1, Eq. (2) can be expanded using six-sublattice magnetic moments as

$$\begin{aligned} F = &-\sum_{i=1}^{6} \boldsymbol{M}_i \cdot \boldsymbol{H} + A(\boldsymbol{M}_1\cdot\boldsymbol{M}_2 + \boldsymbol{M}_2\cdot\boldsymbol{M}_3 + \boldsymbol{M}_3\cdot\boldsymbol{M}_1 \\ &+ \boldsymbol{M}_4\cdot\boldsymbol{M}_5 + \boldsymbol{M}_5\cdot\boldsymbol{M}_6 + \boldsymbol{M}_6\cdot\boldsymbol{M}_4) + B(\boldsymbol{M}_1\cdot\boldsymbol{M}_5 \\ &+ \boldsymbol{M}_1\cdot\boldsymbol{M}_6 + \boldsymbol{M}_2\cdot\boldsymbol{M}_4 + \boldsymbol{M}_2\cdot\boldsymbol{M}_6 + \boldsymbol{M}_3\cdot\boldsymbol{M}_4 \\ &+ \boldsymbol{M}_3\cdot\boldsymbol{M}_5) + \boldsymbol{dt}_{12}\cdot\boldsymbol{M}_1 \times \boldsymbol{M}_2 + \boldsymbol{dt}_{23}\cdot\boldsymbol{M}_2 \times \boldsymbol{M}_3 \\ &+ \boldsymbol{dt}_{31}\cdot\boldsymbol{M}_3 \times \boldsymbol{M}_1 + \boldsymbol{dt}_{45}\cdot\boldsymbol{M}_4 \times \boldsymbol{M}_5 \\ &+ \boldsymbol{dt}_{56}\cdot\boldsymbol{M}_5 \times \boldsymbol{M}_6 + \boldsymbol{dt}_{64}\cdot\boldsymbol{M}_6 \times \boldsymbol{M}_4. \end{aligned} \tag{A1}$$

When the field is applied along the c axis [z axis, $H = (0,0,H)$], each sublattice moment turns to direct as shown in Fig. 10. Using angles shown in the figure, we express the sublattice magnetizations as

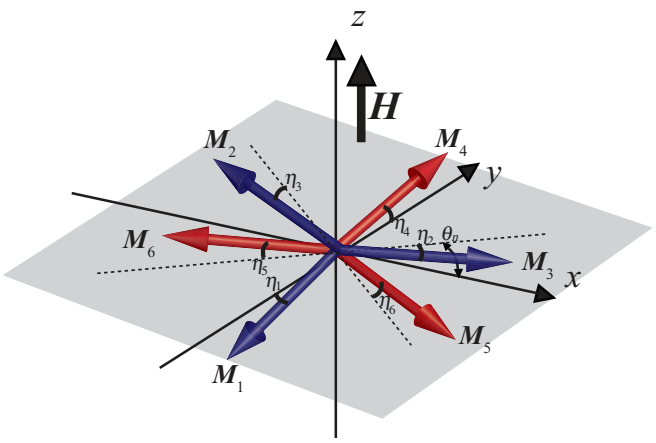

FIG. 10. (Color online) The configuration of the sublattice magnetic moments for $H \| c$.

$$M_n = M_0(\cos\theta_n \cos\eta_n, \sin\theta_n \cos\eta_n, \sin\eta_n), \tag{A2}$$

where $M_0 = (N/6)g\mu_B|S|$. The angles θ_n and η_n are given by

$$\begin{aligned} &\theta_1 = 3\pi/2, \quad \theta_2 = 5\pi/6, \quad \theta_3 = \pi/6, \\ &\theta_4 = \pi/2, \quad \theta_5 = 11\pi/6, \quad \theta_6 = 7\pi/6, \\ &\eta_1 = \eta_2 = \eta_3, \quad \eta_4 = \eta_5 = \eta_6. \end{aligned} \tag{A3}$$

The DM components are given by

$$\begin{aligned} \boldsymbol{dt}_{12} &= \boldsymbol{dt}_{45} = (-\sqrt{3}dt_p/2, -dt_p/2, dt_z), \\ \boldsymbol{dt}_{23} &= \boldsymbol{dt}_{56} = (0, dt_p, dt_z), \\ \boldsymbol{dt}_{31} &= \boldsymbol{dt}_{64} = (\sqrt{3}dt_p/2, -dt_p/2, dt_z). \end{aligned} \tag{A4}$$

By substituting Eqs. (A2), (A3), and (A4) into Eq. (A1), we have

$$\begin{aligned} F = &-H(3M_0\sin\eta_1 + 3M_0\sin\eta_4) \\ &+\tfrac{3}{4}AM_0^2(2 - 3\cos 2\eta_1 - 3\cos 2\eta_4) \\ &+BM_0^2(3\cos\eta_1\cos\eta_4 + 6\sin\eta_1\sin\eta_4) \\ &-\tfrac{3}{2}\sqrt{3}dt_zM_0^2(\cos^2\eta_1 + \cos^2\eta_4) \\ &+\tfrac{3}{2}\sqrt{3}dt_pM_0^2(\sin 2\eta_1 - \sin 2\eta_4). \end{aligned} \tag{A5}$$

The angles η_1 and η_4 are determined by $\partial F/\partial\eta_1 = 0$ and $\partial F/\partial\eta_4 = 0$ numerically. The magnetization M induced along the c axis is expressed as

$$M = 3M_0(\sin\eta_1 + \sin\eta_4). \tag{A6}$$

The transformation of new coordinates $\acute{x}$, $\acute{y}$, and $\acute{z}$ system of the ith sublattice can be performed by the matrix $\mathbf{R}_i$:

$$\mathbf{R}_i = \begin{pmatrix} \cos\theta_i\cos\eta_i & \sin\theta_i\cos\eta_i & \sin\eta_i \\ -\sin\theta_i & \cos\theta_i & 0 \\ -\cos\theta_i\sin\eta_i & -\sin\theta_i\sin\eta_i & \cos\eta_i \end{pmatrix}. \tag{A7}$$

The transformed interaction matrix is such that

$$M_i' = R_i\boldsymbol{M}_i, \quad M_i = R_i^{-1}\boldsymbol{M}_i', \tag{A8}$$

where $\mathbf{R}_i^{-1}$ is the inverse matrix of $\mathbf{R}_i$. The equation of motion of the sublattice moments in the new coordinate can be written as

$$\partial \boldsymbol{M}_i'/\partial t = \gamma \mathbf{R}_i[(\mathbf{R}_i^{-1}\boldsymbol{M}_i') \times (\mathbf{R}_i^{-1}\boldsymbol{H}_i')], \tag{A9}$$

where $\boldsymbol{H}_i' = \mathbf{R}_i H_i$. Expressing Eq. (A9) with the matrix, we have

$$1/\gamma \begin{pmatrix} \partial M'^y_1/\partial t \\ \partial M'^y_2/\partial t \\ \partial M'^y_3/\partial t \\ \partial M'^y_4/\partial t \\ \partial M'^y_5/\partial t \\ \partial M'^y_6/\partial t \\ \partial M'^z_1/\partial t \\ \partial M'^z_2/\partial t \\ \partial M'^z_3/\partial t \\ \partial M'^z_4/\partial t \\ \partial M'^z_5/\partial t \\ \partial M'^z_6/\partial t \end{pmatrix} = \tilde{M} \begin{pmatrix} M'^y_1 \\ M'^y_2 \\ M'^y_3 \\ M'^y_4 \\ M'^y_5 \\ M'^y_6 \\ M'^z_1 \\ M'^z_2 \\ M'^z_3 \\ M'^z_4 \\ M'^z_5 \\ M'^z_6 \end{pmatrix}, \tag{A10}$$

where

$$\tilde{M} = \begin{pmatrix} \tilde{M}_{yy} & \tilde{M}_{yz} \\ \tilde{M}_{zy} & \tilde{M}_{zz} \end{pmatrix}. \tag{A11}$$

Here,

$$\tilde{M}_{yy} = \begin{pmatrix} 0 & -\alpha & \alpha & 0 & \beta & -\beta \\ \alpha & 0 & -\alpha & -\beta & 0 & \beta \\ -\alpha & \alpha & 0 & \beta & -\beta & 0 \\ 0 & \beta' & -\beta' & 0 & \alpha_2 & -\alpha_2 \\ -\beta' & 0 & \beta' & -\alpha_2 & 0 & \alpha_2 \\ \beta' & -\beta' & 0 & \alpha_2 & -\alpha_2 & 0 \end{pmatrix}, \tag{A12}$$

$$\alpha = \frac{M_0}{2}\{dt_p \cos\eta_1 + (\sqrt{3}A - dt_z)\sin\eta_1\}, \tag{A13}$$

$$\alpha_2 = \frac{M_0}{2}\{dt_p \cos\eta_2 + (-\sqrt{3}A + dt_z)\sin\eta_2\}, \tag{A14}$$

$$\beta = \frac{\sqrt{3}}{2} B M_0 \sin\eta_1. \tag{A15}$$

The β' in Eq. (A12) is given by the following replacement:

$$\eta_1 \leftrightarrow \eta_4, \tag{A16}$$

$$\tilde{M}_{yz} = \begin{pmatrix} \gamma & \delta & \delta & 0 & \epsilon & \epsilon \\ \delta & \gamma & \delta & \epsilon & 0 & \epsilon \\ \delta & \delta & \gamma & \epsilon & \epsilon & 0 \\ 0 & \epsilon & \epsilon & \gamma_2 & \delta_2 & \delta_2 \\ \epsilon & 0 & \epsilon & \delta_2 & \gamma_2 & \delta_2 \\ \epsilon & \epsilon & 0 & \delta_2 & \delta_2 & \gamma_2 \end{pmatrix}, \tag{A17}$$

$$\begin{aligned}\gamma = {} & (A + \sqrt{3}dt_z)M_0 \cos^2\eta_1 \\ & - \cos\eta_1 M_0(B\cos\eta_4 + 2\sqrt{3}dt_p \sin\eta_1) \\ & + M_0 \sin\eta_1(-2A\sin\eta_1 - 2B\sin\eta_4) + H\sin\eta_1,\end{aligned} \tag{A18}$$

$$\begin{aligned}\gamma_2 = {} & (A + \sqrt{3}dt_z)M_0 \cos^2\eta_4 \\ & - \cos\eta_4 M_0(B\cos\eta_1 - 2\sqrt{3}dt_p \sin\eta_4) \\ & + M_0 \sin\eta_4(-2A\sin\eta_4 - 2B\sin\eta_1) + H\sin\eta_4,\end{aligned} \tag{A19}$$

$$\begin{aligned}\delta = {} & \frac{M_0}{4}[A - \sqrt{3}dt_z + (3A + \sqrt{3}dt_z)]\cos 2\eta_1 \\ & - 2\sqrt{3}dt_p \sin 2\eta_1,\end{aligned} \tag{A20}$$

$$\begin{aligned}\delta_2 = {} & \frac{M_0}{4}[A - \sqrt{3}dt_z + (3A + \sqrt{3}dt_z)]\cos 2\eta_4 \\ & + 2\sqrt{3}dt_p \sin 2\eta_4,\end{aligned} \tag{A21}$$

$$\epsilon = \frac{B M_0}{2}(2\cos\eta_1 \cos\eta_4 + \sin\eta_1 \sin\eta_4), \tag{A22}$$

$$\tilde{M}_{zy} = \begin{pmatrix} -\gamma & \sigma & \sigma & 0 & \tau & \tau \\ \sigma & -\gamma & \sigma & \tau & 0 & \tau \\ \sigma & \sigma & -\gamma & \tau & \tau & 0 \\ 0 & \tau & \tau & -\gamma_2 & \sigma & \sigma \\ \tau & 0 & \tau & \sigma & -\gamma_2 & \sigma \\ \tau & \tau & 0 & \sigma & \sigma & -\gamma_2 \end{pmatrix}, \tag{A23}$$

$$\sigma = \frac{M_0}{2}(A + \sqrt{3}dt_z), \tag{A24}$$

$$\tau = -\frac{B M_0}{2}, \tag{A25}$$

$$\tilde{M}_{zz} = \begin{pmatrix} 0 & -\alpha & \alpha & 0 & \beta' & -\beta' \\ \alpha & 0 & -\alpha & -\beta' & 0 & \beta' \\ -\alpha & \alpha & 0 & \beta' & -\beta' & 0 \\ 0 & \beta & -\beta & 0 & \alpha_2 & -\alpha_2 \\ -\beta & 0 & \beta & -\alpha_2 & 0 & \alpha_2 \\ \beta & -\beta & 0 & \alpha_2 & -\alpha_2 & 0 \end{pmatrix}. \tag{A26}$$

By substituting Eq. (4) into Eq. (A10), we have

$$(\tilde{M} - i\omega/\gamma \mathbf{E}) \begin{pmatrix} \Delta M_{1\hat{y}} \\ \Delta M_{2\hat{y}} \\ \Delta M_{3\hat{y}} \\ \Delta M_{4\hat{y}} \\ \Delta M_{5\hat{y}} \\ \Delta M_{6\hat{y}} \\ \Delta M_{1\hat{z}} \\ \Delta M_{2\hat{z}} \\ \Delta M_{3\hat{z}} \\ \Delta M_{4\hat{z}} \\ \Delta M_{5\hat{z}} \\ \Delta M_{6\hat{z}} \end{pmatrix} = 0, \tag{A27}$$

where $\mathbf{E}$ is a unit matrix. Theoretical ESR resonance modes in model 1 correspond to the absolute eigenvalues of ω/γ. We obtain the eigenvalues by solving this secular equation.

In the case of the model 2, the angles θ_n and η_n are given by

$$\theta_1 = \pi/2, \quad \theta_2 = 11\pi/6, \quad \theta_3 = 7\pi/6,$$
$$\eta_1 = \eta_2 = \eta_3. \tag{A28}$$

The following calculation process is essentially similar to that for the model 1. By substituting Eqs. (A2), (A4), and (A28) into Eq. (2), we have

$$\begin{aligned} F = & -3HM_0 \sin\eta_1 + \tfrac{3}{4}AM_0^2(1-3\cos 2\eta_1) \\ & -\tfrac{3}{2}\sqrt{3}dt_z M_0^2 \cos^2\eta_1 - \tfrac{3}{2}\sqrt{3}dt_p M_0^2 \sin 2\eta_1 \\ & +\tfrac{3}{4}BM_0^2(1-3\cos 2\eta_1). \end{aligned} \tag{A29}$$

The angle η_1 is determined by $\partial F/\partial\eta_1 = 0$ numerically. The magnetization M induced along the c axis is expressed as

$$M = 3M_0 \sin\eta_1, \tag{A30}$$

where $M_0 = (N/3)g\mu_B|S|$. Theoretical ESR resonance modes for model 2 of the DM model correspond to the absolute eigenvalues for the following matrix:

$$\tilde{M}_{\text{above}} = \begin{pmatrix} 0 & -\alpha_{ab} & \alpha_{ab} & \gamma_{ab} & \beta_{ab} & \beta_{ab} \\ \alpha_{ab} & 0 & -\alpha_{ab} & \beta_{ab} & \gamma_{ab} & \beta_{ab} \\ -\alpha_{ab} & \alpha_{ab} & 0 & \beta_{ab} & \beta_{ab} & \gamma_{ab} \\ \epsilon_{ab} & \chi_{ab} & \chi_{ab} & 0 & -\alpha_{ab} & \alpha_{ab} \\ \chi_{ab} & \epsilon_{ab} & \chi_{ab} & \alpha_{ab} & 0 & -\alpha_{ab} \\ \chi_{ab} & \chi_{ab} & \epsilon_{ab} & -\alpha_{ab} & \alpha_{ab} & 0 \end{pmatrix}, \tag{A31}$$

where

$$\alpha_{ab} = \frac{M_0}{2}\{-dt_p\cos\eta_1 + (\sqrt{3}A + \sqrt{3}B - dt_z)\sin\eta_1\}, \tag{A32}$$

$$\begin{aligned} \beta_{ab} = & \frac{M_0}{4}\{A + B - \sqrt{3}dt_z + (3A + 3B + \sqrt{3}dt_z)\cos 2\eta_1 \\ & + 2\sqrt{3}dt_p \sin 2\eta_1\}, \end{aligned} \tag{A33}$$

$$\begin{aligned} \gamma_{ab} = & M_0\{(A + B + \sqrt{3}dt_z)\cos^2\eta_1 + \sqrt{3}dt_p \sin 2\eta_1 \\ & - 2(A + B)\sin^2\eta_1\} + H\sin\eta_1, \\ \epsilon_{ab} = & \frac{M_0}{2}\{A + B - \sqrt{3}dt_z - (3A + 3B + \sqrt{3}dt_z)\cos 2\eta_1 \\ & - 2\sqrt{3}dt_p \sin 2\eta_1\} - H\sin\eta_1, \end{aligned} \tag{A34}$$

$$\chi_{ab} = \frac{M_0}{2}\{A + B + \sqrt{3}dt_z\}. \tag{A35}$$

We obtain the eigenvalues for the model 2 by solving this secular equation as well.

APPENDIX B

As shown in Sec. IV B, we analyzed experimental results by the CF model using a mean-field approximation as well as the DM model. In this case, we have to consider the new coordinate x', y', z':

$$\left(M_{CFi}^{x'}, M_{CFi}^{y'}, M_{CFi}^{z'}\right) = \mathbf{R}_{CFi}M_i, \tag{B1}$$

where

$$\mathbf{R}_{CFi} = \begin{pmatrix} \cos\theta_{cfi}\cos\eta_{cf} & \sin\theta_{cfi}\cos\eta_{cf} & \sin\eta_{cf} \\ -\sin\theta_{cfi} & \cos\theta_{cfi} & 0 \\ -\cos\theta_{cfi}\sin\eta_{cf} & -\sin\theta_{cfi}\sin\eta_{cf} & \cos\eta_{cf} \end{pmatrix}, \tag{B2}$$

$$\begin{aligned} \theta_{cf1} &= \theta_{cf4} = 3\pi/2, \\ \theta_{cf2} &= \theta_{cf5} = 5\pi/6, \\ \theta_{cf3} &= \theta_{cf6} = \pi/6, \\ \eta_{cf} &= -20\pi/180 = -\pi/9. \end{aligned} \tag{B3}$$

By substituting Eqs. (A2), (A3), and (B1)–(B3) into Eq. (7), we have for the model 1

$$\begin{aligned} F = & -H(3M_0\sin\eta_1 + 3M_0\sin\eta_4) \\ & + \tfrac{3}{4}AM_0^2(2 - 3\sin 2\eta_1 - 3\sin 2\eta_4) \\ & + BM_0^2(3\cos\eta_1\cos\eta_4 + 6\sin\eta_1\sin\eta_4) \\ & + 3KM_0^2[\sin^2(\eta_1 - \eta_{cf}) + \sin^2(\eta_4 + \eta_{cf})] \\ & - 3CM_0^2[\cos^2(\eta_1 - \eta_{cf}) - \cos^2(\eta_4 + \eta_{cf})]. \end{aligned} \tag{B4}$$

For the model 2, the free energy F can be written as

$$\begin{aligned} F = & -3HM_0\sin\eta_1 + \tfrac{3}{4}AM_0^2(1 - 3\cos 2\eta_1) \\ & + \tfrac{3}{4}BM_0^2(1 - 3\cos 2\eta_1) + 3KM_0^2\sin^2(\eta_{cf} + \eta_1) \\ & - 3CM_0^2\cos^2(\eta_{cf} + \eta_1). \end{aligned} \tag{B5}$$

We calculate theoretical ESR resonance modes for the CF model by an essentially similar method to Appendix A.

*Present address: College of Integrated Arts and Science, Osaka Prefecture University, Sakai 599-8531, Japan.
†Present address: Institute for Materials Research, Tohoku University, 2-1-1 Katahira, Sendai 980-8577, Japan.
‡Present address: Institute for Materials Science and Graduate School of Pure and Applied Sciences, University of Tsukuba, 1-1-1 Tennodai, Tsukuba Ibaraki 305-8573, Japan.
§hagiwara@cqst.osaka-u.ac.jp

[1] M. B. Hastings, Phys. Rev. B **63**, 014413 (2000).
[2] Y. Ran, M. Hermele, P. A. Lee, and X. G. Wen, Phys. Rev. Lett. **98**, 117205 (2007).
[3] S. Sachdev, Phys. Rev. B **45**, 12377 (1992).
[4] T. Hikihara, L. Kecke, T. Momoi, and A. Furusaki, Phys. Rev. B **78**, 144404 (2008).
[5] J. Sudan, A. Lüscher, and A. M. Läuchli, Phys. Rev. B **80**, 140402(R) (2009).
[6] T. Sakakibara, T. Tayama, Z. Hiroi, K. Matsuhira, and S. Takagi, Phys. Rev. Lett. **90**, 207205 (2003).

[7]M. J. Harris, S. T. Bramwell, D. F. McMorrow, T. Zeiske, and K. W. Godfrey, Phys. Rev. Lett. **79**, 2554 (1997).
[8]D. A. Huse and A. D. Rutenberg, Phys. Rev. B **45**, 7536 (1992).
[9]A. B. Harris, C. Kallin, and A. J. Berlinsky, Phys. Rev. B **45**, 2899 (1992).
[10]F. Mila, Phys. Rev. Lett. **81**, 2356 (1998).
[11]F. Bert, D. Bono, P. Mendels, F. Ladieu, F. Duc, J.-C. Trombe, and P. Millet, Phys. Rev. Lett. **95**, 087203 (2005).
[12]P. W. Anderson, Mater. Res. Bull. **8**, 153 (1973).
[13]Y. Narumi, K. Katsumata, Z. Honda, J.-C. Domenge, P. Sindzingre, C. Lhuillier, Y. Shimaoka, T. C. Kobayashi, and K. Kindo, Europhys. Lett. **65**, 705 (2004).
[14]F. Bert, S. Nakamae, F. Ladieu, D. L'Hote, P. Bonville, F. Duc, J.-C. Trombe, and P. Mendels, Phys. Rev. B **76**, 132411 (2007).
[15]G. Misguich, and P. Sindzingre, Eur. Phys. J. B **59**, 305 (2007).
[16]P. Mendels, F. Bert, M. A. de Vries, A. Olariu, A. Harrison, F. Duc, J. C. Trombe, J. S. Lord, A. Amato, and C. Baines, Phys. Rev. Lett. **98**, 077204 (2007).
[17]P. Mendels and F. Bert, J. Phys. Soc. Jpn. **79**, 011001 (2010).
[18]Z. Hiroi, M. Hanawa, N. Kobayashi, M. Nohara, H. Takagi, Y. Kato, and M. Takigawa, J. Phys. Soc. Jpn. **70**, 3377 (2001).
[19]S. Yamashita, T. Moriura, Y. Nakazawa, H. Yoshida, Y. Okamoto, and Z. Hiroi, J. Phys. Soc. Jpn. **79**, 083710 (2010).
[20]Y. Okamoto, H. Yoshida, and Z. Hiroi, J. Phys. Soc. Jpn. **78**, 033701 (2009).
[21]W. Zhang, H. Ohta, W. Zhang, S. Okubo, M. Fujisawa, T. Sakurai, Y. Okamoto, H. Yoshida, and Z. Hiroi, J. Phys. Soc. Jpn. **79**, 083710 (2010).
[22]K. Morita, M. Yano, T. Ono, H. Tanaka, K. Fujii, H. Uekusa, Y. Narumi, and K. Kind, J. Phys. Soc. Jpn. **77**, 043707 (2008).
[23]T. Ono, K. Morita, M. Yano, H. Tanaka, K. Fujii, H. Uekusa, Y. Narumi, and K. Kindo, Phys. Rev. B **79**, 174407 (2009).
[24]K. Matan, T. Ono, Y. Fukumoto, T. J. Sato, J. Yamaura, M. Yano, K. Morita, and H. Tanaka, Nat. Phys. **6**, 865 (2010).
[25]D. Grohol, D. G. Nocera, and D. Papoutsakis, Phys. J. B **67**, 064401 (2003).
[26]T. Inami, M. Nishiyama, S. Maegawa, and Y. Oka, Phys. Rev. B **61**, 12181 (2000).
[27]A. S. Wills, A. Harrison, C. Ritter, and R. I. Smith, Phys. Rev. B **61**, 6156 (2000).
[28]D. G. Nocera, B. M. Barlett, D. Grohol, D. Papoutsakis, and M. P. Shores, Chem. Eur. J. **10**, 3850 (2004).
[29]D. Grohol, K. Matan, J. Cho, S. Lee, J. W. Lynn, D. G. Nocera, and Y. S. Lee, Nat. Mater. **4**, 323 (2005).
[30]M. Elhajal, B. Canals, and C. Lacroix, Phys. Rev. B **66**, 014422 (2002).
[31]K. Matan, D. Grohol, D. G. Nocera, T. Yildirim, A. B. Harris, S. H. Lee, S. E. Nagler, and Y. S. Lee, Phys. Rev. Lett. **96**, 247201 (2006).
[32]K. Matan, B. M. Bartlett, J. S. Helton, V. Sikolenko, S. Mat'aš, K. Prokes, Y. Chen, J. W. Lynn, D. Grohol, T. J. Sato, M. Tokunaga, D. G. Nocera, and Y. S. Lee, Phys. Rev. B **83**, 214406 (2011).
[33]M. G. Townsend, G. Longworth, and E. Roudaut, Phys. Rev. B **33**, 4919 (1986).
[34]H. Tanaka, Y. Kahawa, T. Hasegawa, M. Igarashi, S. Teraoka, K. Ito, and R. P. Singh, J. Phys. Soc. Jpn. **58**, 2930 (1989).
[35]Y. Miyajima, H. Yashiro, T. Kashiwagi, M. Hagiwara, and H. Hori, J. Phys. Soc. Jpn. **73**, 280 (2004).
[36]T. Moriya, Phys. Rev. **120**, 91 (1960).
[37]T. Yildirim and A. B. Harris, Phys. Rev. B **73**, 214446 (2006).
[38]A. Zorko, S. Nellutla, J. van Tol, L. C. Brunel, F. Bert, F. Duc, J.-C. Trombe, M. A. de Vries, A. Harrison, and P. Mendels, Phys. Rev. Lett. **101**, 026405 (2008).
[39]T. Morimoto, M. Nishiyama, S. Maegawa, and Y. Oka, J. Phys. Soc. Jpn. **72**, 2085 (2003).
[40]M. Leblanc, R. De Pape, G. Ferey, and J. Pannetier, Solid State Commun. **58**, 171 (1986).
[41]O. Cépas, C. M. Fong, P. W. Leung, and C. Lhuillier, Phys. Rev. B **78**, 140405(R) (2008).